ACS NANO

www.acsnano.org

ARTICLE

# Metal–Insulator Transition of Single-Crystal $V_2O_3$ through van der Waals Interface Engineering

Jie Jiang,*,# Lifu Zhang,# Yang Hu, Yuwei Guo, Zhizhong Chen, Ru Jia, Saloni Pendse, Yu Xiang, Gwo-Ching Wang, Yunfeng Shi,* and Jian Shi*

Cite This: *ACS Nano* 2023, 17, 11783–11793

Read Online

ACCESS | Metrics & More | Article Recommendations | Supporting Information

**ABSTRACT:** Strongly correlated electron materials harbor interesting materials physics, such as high-$T_c$ superconductivity, colossal magnetoresistance, and metal–insulator transition. These physical properties can be greatly influenced by the dimensionality and geometry of the hosting materials and their interaction strengths with underlying substrates. In a classic strongly correlated oxide vanadium sesquioxide ($V_2O_3$), the coexistence of a metal–insulator and paramagnetic-antiferromagnetic transitions at ∼150 K makes this material an excellent platform for exploring basic physics and developing future devices. So far, most studies have been focused on epitaxial thin films in which the strongly coupled substrate has a pronounced effect on $V_2O_3$, leading to the observations of intriguing phenomena and physics. In this work, we unveil the kinetics of a metal–insulator transition of $V_2O_3$ single-crystal sheets at nano and micro scales. We show the presence of triangle-like alternating metal/insulator phase patterns during phase transition, which is drastically different from the epitaxial film. The observation of single-stage metal–insulator transition in $V_2O_3$/graphene compared to the multistage in $V_2O_3/SiO_2$ evidence the importance of sheet–substrate coupling. Harnessing the freestanding form of the $V_2O_3$ sheet, we show that the phase transition of $V_2O_3$ sheet can generate a large dynamic strain to monolayer $MoS_2$ and tune its optical property based on the $MoS_2/V_2O_3$ hybrid structure. The demonstration of the capability in tuning phase transition kinetics and phase patterns using designed hybrid structure of varied sheet–substrate coupling strengths suggests an effective knob in the design and operation of emerging Mott devices.

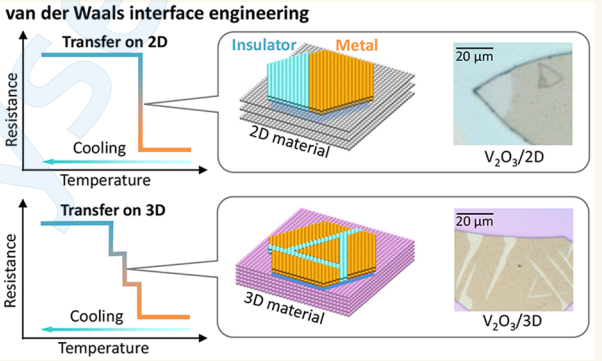


**KEYWORDS:** *metal–insulator transition, vanadium sesquioxide, domain pattern, van der Waals interface, 2D/3D hybrid structure, strain effect*



For thin films or two-dimensional materials, their couplings with the underlying substrates have been found to be critical to affecting their phase stability and physical properties. Substrates could impose large lattice strains,[1] change the dielectric environment,[2] and tune the electron–phonon interactions of the films.[3,4] This could lead to substantial enhancements of order parameters in ferroelectrics,[1,5−7] multiferroics,[8,9] and superconductors.[10−12] So far, in understanding the materials' physics of strongly correlated materials at reduced dimension, most studies have been focused on epitaxial thin films in which substates (interfaces) have a substantial influence on the materials' properties.[3,4,13−15] When the substrate is removed or a weakly coupled interface (e.g., van der Waals interface) exists instead, discoveries could arise. For example, the synthesis of a single crystalline free-standing $VO_2$ nanowire has enabled the direct observations of intriguing domain structures,[16,17] M1 and M2 phases,[18,19] photothermal response[20] and anomalously low electronic thermal conductivity.[21] The fabrication of free-standing perovskite oxides film such as $BiFeO_3$[22] and $BaTiO_3$[23] has led to the discovery of giant polarization (monolayer) and superelasticity.

Bulk $V_2O_3$ is a prototypical Mott insulator, which undergoes a first-order metal–insulator transition from an $\alpha$-corundum

Received: March 22, 2023
Accepted: June 8, 2023
Published: June 12, 2023

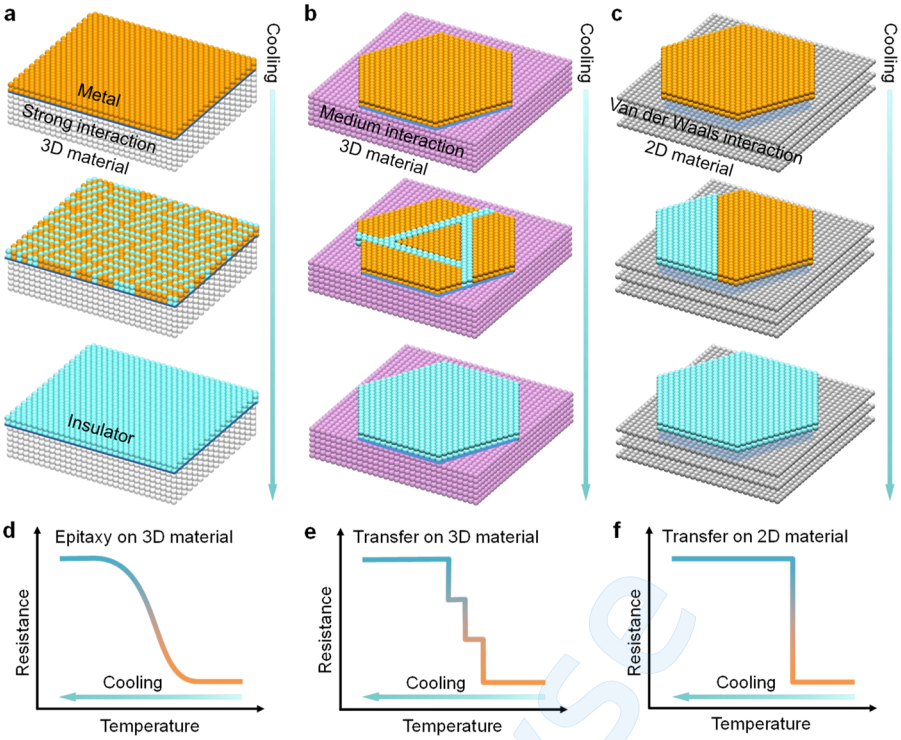


**Figure 1. Effect of interfacial interaction on metal−insulator transition in $V_2O_3$. a, Schematic of the metal−insulator transition in a $V_2O_3$ epitaxial thin film during cooling when a 3D material is used as substrate. Strong interaction is expected between the film and the 3D substrate. The middle panel shows possible massive striped insulating domains (nanoscale) formed during the transition. b, Schematic of the metal−insulator transition in a $V_2O_3$ sheet during cooling when the sheet is mechanically transferred on a 3D material. Medium interaction is expected between the transferred sheet and the 3D substrate. The middle panel shows possible multiple striped insulating domains formed during the transition. c, Schematic of the metal−insulator transition in a $V_2O_3$ sheet during cooling when the sheet is mechanically transferred on a 2D material. van der Waals interaction is formed between the transferred sheet and 2D substrate. The middle panel shows a possible single insulating domain formed during the transition. White: 3D material for epitaxy, purple: 3D material for transfer, gray: 2D material, orange: metallic phase, light cyan: insulating phase, dark blue lines: strong interaction, blue lines: medium interaction, light blue lines: van der Waals interaction. d, Resistance switching (continuous) in the epitaxial film on 3D substrate during cooling. e, Resistance switching (multiple-stage discrete changes) in the transferred sheet on a 3D substrate during cooling. f, Resistance switching (single-stage sharp change) in the transferred sheet on a 2D substrate during cooling.**

paramagnetic metal (high-temperature phase) to a monoclinic antiferromagnetic insulator (low-temperature phase) with a transition temperature $T_c$ of ∼150 K.[24−27] The phase transition in $V_2O_3$ has been a subject of intensive theoretical and experimental studies in early decades[28,29] and has been revisited in recent years.[30−32] The transition temperature can be tuned by pressure, doping, photoexcitation, and electric field.[33−37] Although the details of electrodynamics of $V_2O_3$ remain debatable,[38−43] it is agreed that electron−electron interactions are partially responsible for the insulating state. Under the Mott-Hubbard picture, the intraatomic Coulomb repulsion splits half-filled $t_{2g}$ band into an empty upper Hubbard band and a filled lower Hubbard band, resulting in an insulating state.

$V_2O_3$ bulk crystal exhibits a sharp metal−insulator transition.[27] However, its epitaxial thin film shows a continuous transition due to the existence of massive heterogeneous nucleation sites and crystallographic defects.[31,32,44−46] $V_2O_3$ nanowires, fabricated by plasma etching on epitaxial thin films, exhibit multiple-stage resistance changes during the metal−insulator transition,[47,48] reflecting the number of nucleation sites in the small nanowire. Recently, nanoresolved infrared microscopy[31] and X-ray photoemission electron microscopy[44,45] have revealed the real-space evolution of a striped multiple-domain pattern in thin films during the phase transition. The multiple-domain pining phenomenon in these thin films[44,45] is likely due to defects which lead to low nucleation barrier possibly because of a strong film−substrate interaction. Scanning photoelectron microscopy has revealed the formation of a trigonal-shaped domain in Cr-doped $V_2O_3$.[49] The intrinsic domain pattern (not defect-controlled) in $V_2O_3$ with a low-dimensional geometry has been unknown. Understanding the intrinsic domain evolution of an archetypal Mott insulator is of paramount importance for the design and development of emerging Mott devices.[50]

Here to understand and tune the phase transition in $V_2O_3$, we apply substrate (interface) engineering. Figures 1a−c show the phase (domain) evolution for the $V_2O_3$ epitaxial thin film (a) and sheets (b,c) (having a hexagon-like structure) during cooling with strong chemical epitaxial interaction, coupling from mechanically constructed interface with three-dimensional (3D) substrate (medium interaction), and weak (van der Waals) interaction from mechanically constructed interface with 2D substrate, respectively. It is expected that the material−substrate interaction strength reduces from the epitaxial interface (Figure 1a) to mechanical interface (Figure 1b) to van der Waals interface (Figure 1c).[51−53] For the epitaxial interface (e.g., $V_2O_3$ on c-plane sapphire), massive observations show that the transition is continuous reflected by the continuous change of resistance (Figure 1d), and the


https://doi.org/10.1021/acsnano.3c02649
ACS Nano 2023, 17, 11783−11793

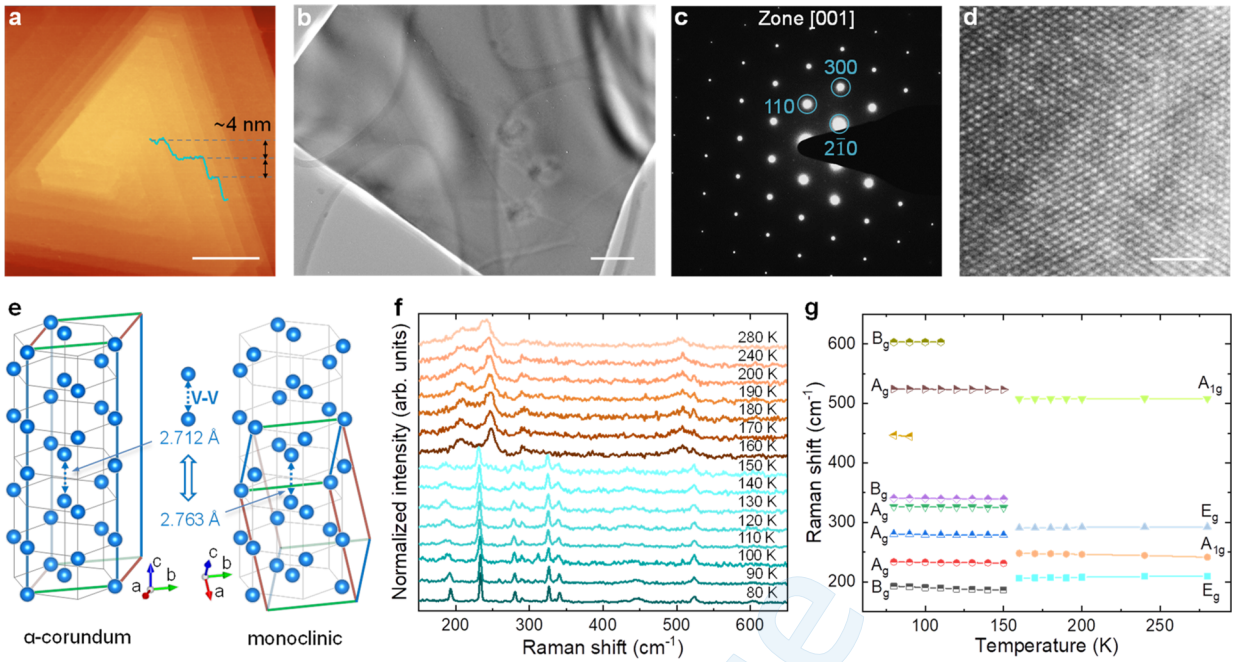


**Figure 2. Morphology and structural analysis of single-crystal $V_2O_3$ sheets. a, AFM image of a $V_2O_3$ sheet. b–d, TEM image (b), diffraction pattern (c) and high-resolution TEM image (d) of a $V_2O_3$ sheet. e, Schematic of atomic structures of $\alpha$-corundum (metallic) and monoclinic (insulating) phases of $V_2O_3$. The pseudohexagonal unit cell and primitive unit cell are outlined in red, green, and blue lines. The black and gray hexagons are guides for the eyes. f,g, Temperature-dependent (80–280 K) Raman spectra (f) and vibration modes (g) of a $V_2O_3$ sheet, revealing a structural phase transition with a $T_c$ of ~150 K. Scale bars in a: 5 $\mu$m, b: 200 nm, d: 2 nm.**

domain shape does not follow the intrinsic hexagon-like structure of $V_2O_3$.[31] Based on the recent understanding of the metal–insulator transition revealed in $VO_2$ nanowires when interfaced with weak-coupled substrates or at free-standing form, it is expected that in the case of medium interaction, it is possible that the metal–insulator transition proceeds at multiple discrete stages that could give multiple-stage discrete sharp resistance changes (Figure 1e). In the case of van der Waals interaction, a single-stage transition may occur, leading to a single-stage sharp resistance change (Figure 1f). The material–substrate coupling strength is an effective tuning knob of the phase transition in $V_2O_3$.

Experimentally revealing the metal–insulator transition kinetics demands the careful design and development of controlled material-substrate interfaces. Here, to develop $V_2O_3$-based van der Waals and non-van der Waals interfaces, using flux method (see Methods and SI Figure S1), we synthesize single-crystal $V_2O_3$ sheets at nano and micro scales. We then developed $V_2O_3$ heterostructures by mechanically transferring oxide sheets onto few-layer graphene (FLG), muscovite mica, $SiO_2$/Si and $CaF_2$, or $MoS_2$ on $V_2O_3$ sheets. With microscopy, spectroscopy, and transport measurements, we have observed varied metal–insulator transition dynamics in different heterostructures. In the $MoS_2/V_2O_3$ heterostructure, we find that the structural phase transition of $V_2O_3$ could generate a dynamic strain in the $MoS_2$ monolayer that leads to the tuning of its photoluminescent property. The demonstration of these high quality $V_2O_3$ heterostructures and our approach open a window in designing and developing future Mott heterostructures.

## RESULTS AND DISCUSSION

The as-grown single-crystal $V_2O_3$ sheets have lateral sizes ranging from tens of micrometers up to millimeters, as shown in optical microscopy images of SI Figures S2a–l, 3a–l. The surfaces of these sheets exhibit features of equilateral triangles or hexagons (e.g., SI Figures S2m, 3f). These features could be related to the pseudohexagonal structure of metallic phase of $V_2O_3$ at room temperature. The atomic force microscopy (AFM) images and their corresponding height profiles in SI Figures S4a–j show sheets with thicknesses ranging from a hundred nanometers up to a few micrometers. Figure 2a is an AFM image at the center of the equilateral triangle in SI Figure S2m, revealing a screw-dislocation-driven growth mode.

We characterize the crystal structure of as-grown $V_2O_3$ sheets to be the $\alpha$-corundum phase by using X-ray diffraction (XRD) measurement (SI Figure S5a). The out-of-plane direction of the sheet is [001] (SI Figure S5b). Figures 2b,c, and SI Figure S6a,f show transmission electron microscopy (TEM) images and the corresponding diffraction patterns for different sheets, confirming their $\alpha$-corundum phases. The high-resolution TEM images (Figure 2d and SI Figure S7a) clearly illustrate the pseudohexagonal lattice of $V_2O_3$. The fast Fourier transform (FFT) pattern (SI Figure S7b) and inverse FFTs (based on their inset patterns with a marked white spot to highlight lattice fringes) (SI Figures S7c,d) illustrate the single crystal nature of the sheets.

Figure 2e shows the pseudohexagonal unit cell of the $\alpha$-corundum phase containing six $V_2O_3$ formula units (left panel) and primitive unit cell of the monoclinic phase containing four $V_2O_3$ formula units (right panel). These two structures exhibit sharply different lattice dynamics (e.g., Raman scattering). Thus, we investigate the structural phase transition in a $V_2O_3$ sheet by a Raman measurement. Figures 2f and g show Raman spectra of the sheet measured from 80 to 280 K and frequency shifts of all scattering peaks as a function of temperature, respectively. The abrupt changes in the Raman spectrum (lightest cyan spectrum at 150 K compared to the darkest red


https://doi.org/10.1021/acsnano.3c02649
ACS Nano 2023, 17, 11783–11793

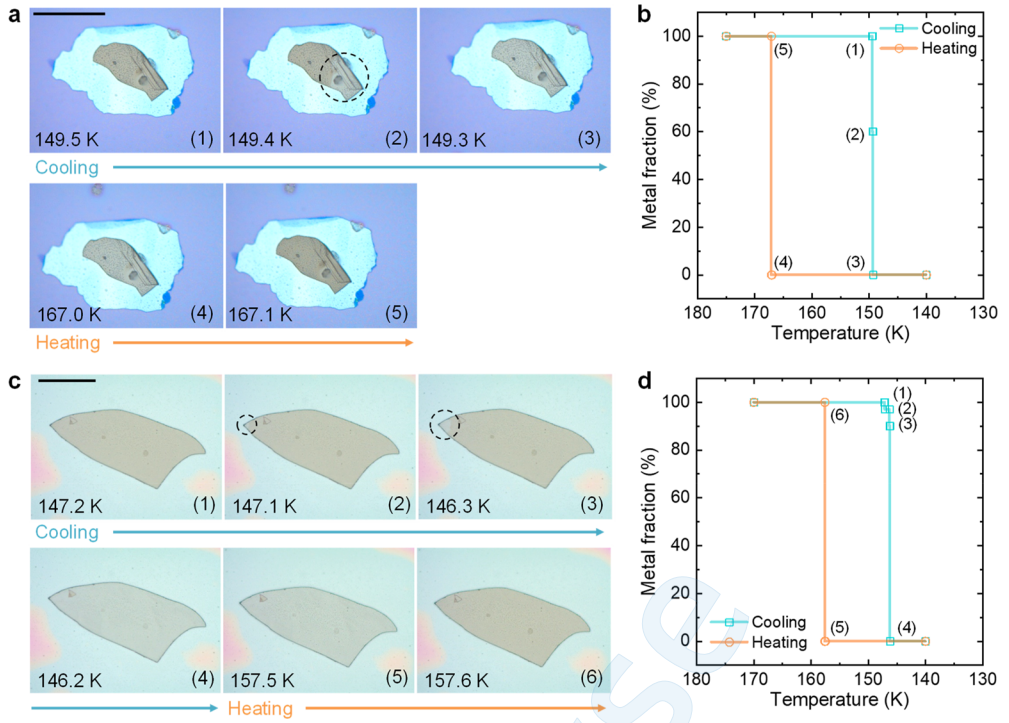


**Figure 3. Metal−insulator domain evolutions of single-crystal $V_2O_3$ sheets on few-layer graphene (a,b) and mica (c,d). a,c, Optical microscopy images and b,d, metal fraction as a function of temperature during cooling and heating. The $V_2O_3$ sheet and FLG (a) are transferred onto a $SiO_2$/Si substrate subsequently. The dark color in the sheet corresponds to its metallic phase, while the light one corresponds to its insulating phase. The initial insulating nucleus is circled by the black dashed circle in a. The data points (1)−(5) in b and (1)−(6) in d are calculated from the corresponding images in a and c, respectively. The cooling and heating rate are kept at 1 K/min. Scale bars in a: 50 $\mu$m; c: 100 $\mu$m.**

one at 160 K, Figure 2f) and scattering peak positions at 150 K (Figure 2g) clearly indicate a structural phase transition. The scattering peaks at 186.3 and 339.4 $cm^{-1}$, peaks at 231.5 $cm^{-1}$, 278.7 and 325.0 $cm^{-1}$ and peak at 603.3 $cm^{-1}$ (150 K) could be assigned to $B_g$, $A_g$ and $E_g$ modes, respectively, for the $\alpha$-corundum phase.[54] The scattering peaks at 206.5 and 290.8 $cm^{-1}$ and peaks at 248.2 and 507.5 $cm^{-1}$ could be assigned to $E_g$ and $A_{1g}$ modes, respectively, for the monoclinic phase.[54] It is noted that a laser (with the illumination wavelength at 532 nm) with a low intensity is used during the measurements to avoid the laser heating-induced phase transition (SI Figure S8).

The $\alpha$-corundum-monoclinic (metal−insulator) transition in $V_2O_3$ crystals can be investigated by optical microscopy based on the different optical properties of the metallic and insulating phases.[38,40] However, in contrast to $VO_2$,[16,17,55] the different color contrast under optical microscope between the metallic and insulating domains/phases in $V_2O_3$ had not been reported. This may be because the thin films have domains only at the nanoscale due to their strong interactions with the substrates.[31] Here, in our single-crystal $V_2O_3$ sheets transferred on different substrates (by using a dry transfer technique, see Methods), we observe a color change from dark yellow to light yellow (metal to insulator) when the temperature is lowered across $T_c$ (Figures 3a−d, Figures 4a−d and SI Figures S9−11a,b). During cooling, for the sheets transferred on FLG (Figures 3a,b) and mica (Figures 3c,d, and Video S1) that have van der Waals-like interfaces, we observe single nuclei, and their metal−insulator transitions are completed within 0.1 K (Figure 3a(2,3)) and 1.1 K (Figure 3c(2−4)) (0.1 K is the test limit), respectively. However, for the sheets transferred on $SiO_2$/Si (Figures 4a−d and SI Figures S9a,b) and $CaF_2$ (SI Figures S10a,b, and 11a,b, and Videos S2 and S3) that have medium sheet−substrate interactions (much weaker than the epitaxial thin film−substrate interaction but stronger than the van der Waals interaction), we observe multiple nuclei and their transitions are completed within 40.0 K (Figure 4c(2−7)), 14.4 K (SI Figure S9a(2−10)), 6.9 K (SI Figure S10a(2−8)), and 5.8 K (SI Figure S11a(2−8)), respectively. Here, the different transition temperatures for the sheets transferred on the same substrate may be caused by some other parameters, such as the size of the sheet.

Particularly, the sheet in Figure 4a (enlarged views of white dashed rectangles in Figure 4c(1, 3−7)) shows striped (insulating) domains with a trigonal arrangement during cooling. Figure 4b is a schematic of this trigonal striped domain pattern. These striped domains have lengths of tens of micrometers and widths of a few micrometers. Their sizes are much larger than that in epitaxial thin films.[31,44] The trigonal arrangement could be due to the pseudohexagonal structure of the metallic phase of $V_2O_3$. Meanwhile, some domains nucleate at the edge of the sheet and grow larger until they merge together during cooling (Figure 4c(1−7)). During heating, however, fewer domains nucleate (no striped domains) and the growth is much faster (Figure 4c(8−14)). Figure 4d plots the metal fraction as a function of temperature, in which data points are obtained from Figure 4c(1−14). It clearly illustrates the multiple states during phase transition. SI Figure S12a,b shows a second measurement (cooling and heating) for the same sheet. We observe a similar trigonal striped domain pattern. It is noticed that these striped domains do not locate at the same position as those in Figure 4c. The different positions of striped domains between two measurements


https://doi.org/10.1021/acsnano.3c02649
ACS Nano 2023, 17, 11783−11793

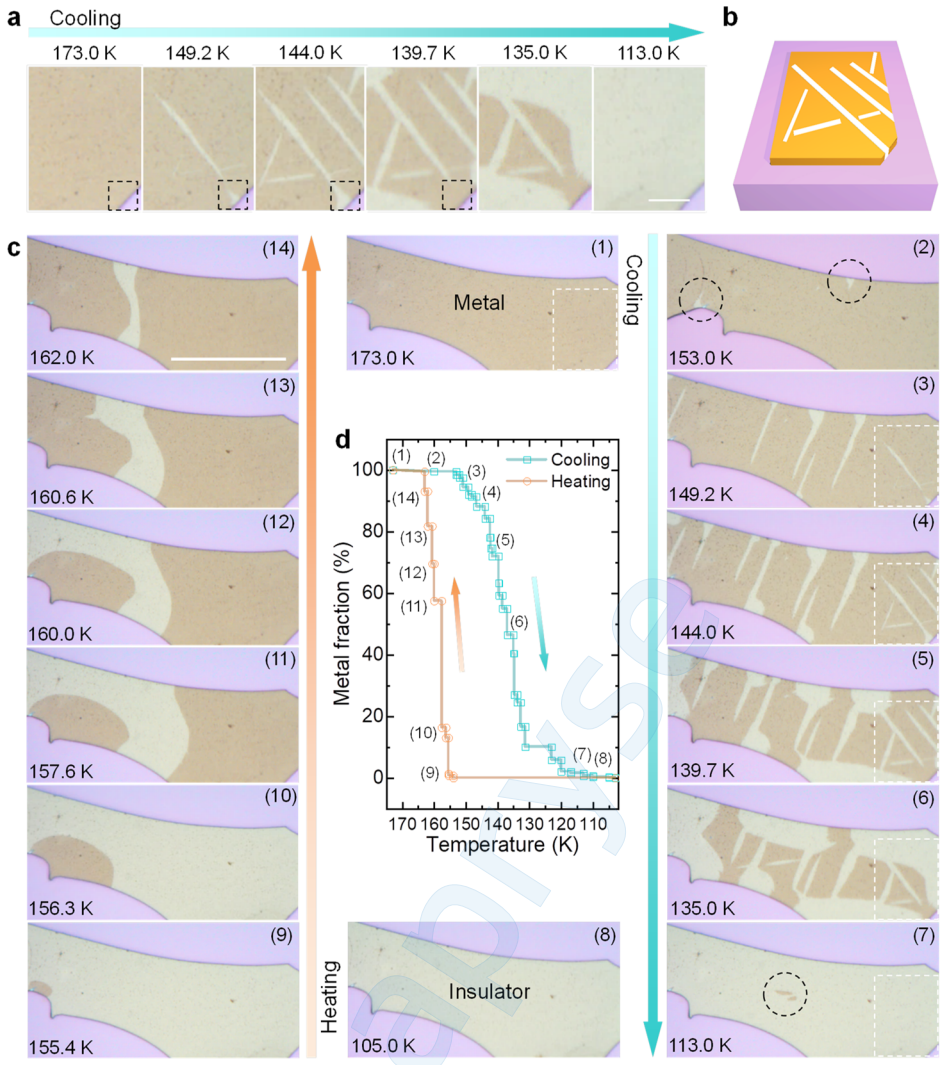


**Figure 4. Metal−insulator domain evolution of a single-crystal $V_2O_3$sheet on $SiO_2$/Si. a, Optical microscopy images (selected areas, white dashed rectangles in c) of a $V_2O_3$ sheet during the metal−insulator transition (cooling), revealing a trigonal striped (insulating) domain pattern. The insulating domain in black dashed squares switches back to the metallic phase. b, Schematic of the domain pattern. c, Optical microscopy images of the sheet during the phase transition (cooling and heating). The dark color represents the metallic phase, while the light color represents the insulating phase. The initial insulating nuclei in c (2) and last metallic domain in c (7) in black dashed circles indicate a supercooling of the metallic domain up to 40 K. The plot at the central panel shows the metal fraction as a function of temperature extracted from the optical microscopy images. The data points of (1)−(14) are obtained from the corresponding images in c. The cooling and heating rate are kept at 1 K/min. Scale bars in a: 10 $\mu$m; b: 50 $\mu$m.**

suggest that the nucleation is a stochastic process here (not defect-controlled). We need to mention that the cooling and heating rate was kept at 1 K/min for all samples and devices (except as specified) and the phase transition of each single step should occur in subnanoseconds.[32]

The single-domain and multiple-domain behaviors (trigonal stripped domain pattern) in the $V_2O_3$ sheets transferred on different substrates indicate that the formation and thermodynamic stability of domains and the kinetics of metal−insulator transition could be greatly affected by sheet−substrate interactions (substrate clamping effect).[55] The periodic domain pattern has been widely observed in epitaxial ferroelectric[56−59] and magnetic films[60−63] and strained $VO_2$ nanobeams.[16,17,55,64] The formation of the periodic domain pattern reduces the strain energy of the material-substrate system at the cost of increasing the domain-wall energy. When $V_2O_3$ changes from an $\alpha$-corundum to a monoclinic (metallic to insulating) phase, the lattice constants along $a$ and $b$ of the metallic phase expand by 0.74% and 1.22%, respectively. The expansion of the insulating domain induces compressive stress on the nearby metallic domains. This compressive stress could stabilize the metallic phase, leading to a downward shift of $T_c$. The formed (insulating) domain may switch back to the original state (black dashed squares in Figure 4a), consistent with our MD simulations (bottom panels in Figure 2a). This back-switching is probably due to a local compressive stress induced by expansions of nearby switched domains. Without (or with very weak) sheet−substrate interaction, the periodic domain pattern is not needed since the substrate-imposed strain is absent (or extremely weak), which is reflected in e.g., suspended $VO_2$ nanobeams[17,55] and our transferred $V_2O_3$ sheets on FLG and mica (Figures 3a−d, Figures 4a−d, respectively). The sheet−substrate interaction in transferred $V_2O_3$ sheets on $SiO_2$/Si may be relieved after cooling, as indicated by buckling of the sheet in SI Figure S12b(7),(8). Thus, the striped domain is not formed during heating (Figure


https://doi.org/10.1021/acsnano.3c02649
ACS Nano 2023, 17, 11783−11793

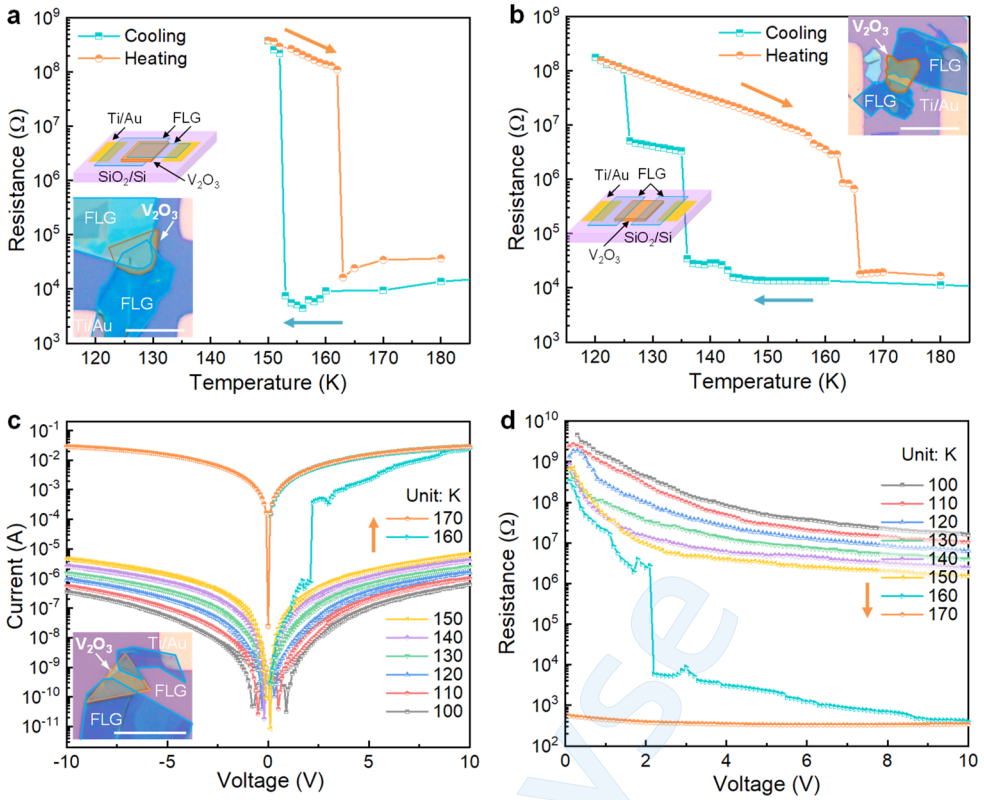


**Figure 5. Resistance jumps in single-crystal $V_2O_3$ sheets. a,b, Resistance as a function of temperature for a vertical device (device #1) (a) and a planar device (device #2) (b), revealing the temperature driven metal−insulator transitions. Insets of a and b are optical microscopy images (corner) and schematics (middle-left) of devices #1 and #2 (FLG/$V_2O_3$/FLG), respectively. The $V_2O_3$ sheets and FLGs are outlined by orange and blue lines, respectively. c,d, Logarithmic current (c) and resistance (d) as a function of voltage of a planar device (device #3). Inset is an optical image of device #3. Unedited optical images of devices #1−3 can be found in the insets of SI Figures S14a−c. Scale bars in the insets of a−c: 20 $\mu$m.**

4c(8−14) and SI Figure S12b(8−14)). This asymmetric transition behavior between heating and cooling can also be observed in SI Figures S9−11a,b.

In addition, during cooling, we notice that the initial insulating nuclei in the $V_2O_3$ sheet occur at 153 K (Figure 4c(2)) and the metallic domains remain at 113 K (Figure 4c(7)), suggesting a supercooling of the metallic domain up to 40.0 K. This supercooling may be due to the existence of compressive strain fields in the sheet.[55] For the second cooling−heating cycle, the maximum supercooling of the metallic domain (SI Figure S12b(2),(7)) decreases to 31.2 K. This decrease may result from the relief of the sheet−substrate interaction. For the sheets transferred on 2D materials, due to their van der Waals interactions, the supercooling of the metallic domain is expected to be much lower. Indeed, we observe negligible supercooling of 0.1 K in the sheet on FLG and 1.1 K on mica, as shown in Figures 3a,b and Figures 3c,d, respectively.

To help understand the experimental observations on domain evolutions of a crystalline sheet on substrates with different interactions, we apply molecular dynamics (MD) simulations in which we use a simple single-element system which exhibits displacive solid phase transition for the purpose of illustrations (see details in Methods, Supporting Discussion, SI Figures S13a−e and Videos S4 and S5). These MD simulations, although the used single-element system is different from the complex crystal structures of $V_2O_3$, demonstrate a similar effect of sheet−substrate interaction on the structural phase transition dynamics as the experimental case of $V_2O_3$.

Across the $\alpha$-corundum-monoclinic transition of $V_2O_3$, the symmetry (space group $R\bar{3}c$, 167) of the $\alpha$-corundum phase is broken, and V−V dimers elongate (Figure 2e). Under the Peierls distortion view, the elongation of V−V dimers affects the degeneracy of $e_g^{\pi}$ and $e_g^{\pi*}$ orbitals and the energy levels of $e_g^{\pi}$ and $a_{1g}$ orbitals, respectively, resulting in the insulating behavior.[43,44,65] To characterize the electronic phase transition of $V_2O_3$, we have fabricated $V_2O_3$ sheet-based two-terminal devices with FLGs as electrical contacts (FLG/$V_2O_3$/FLG) by using the dry transfer technique (see Methods). Here, transferred FLGs instead of deposited metals are used as electrodes to minimize the mechanical clamping effect from deposited films such as Au. The optical microscopy images in the insets of Figures 5a,b,c (black dashed rectangles in SI Figures S14a,b,c) and SI Figures S15a,c,16a,c show the fabricated devices (named #1−#7, respectively). The temperature-dependent resistance measurements in Figures 5a,b (devices #1, #2) and SI Figures S15b,d,16b,d (devices #4−#7) exhibit a distinct metal−insulator transition. The resistances show a single jump during cooling and heating in Figure 5a (up to 4 orders of magnitude) and SI Figures S15b,d, while the resistances show multiple jumps in Figure 5b and SI Figures S16b,d. We need to mention that the magnitudes of resistance hysteresis are varied in different devices probably due to the varied contact resistances introduced during the transfer process.



https://doi.org/10.1021/acsnano.3c02649
ACS Nano 2023, 17, 11783−11793

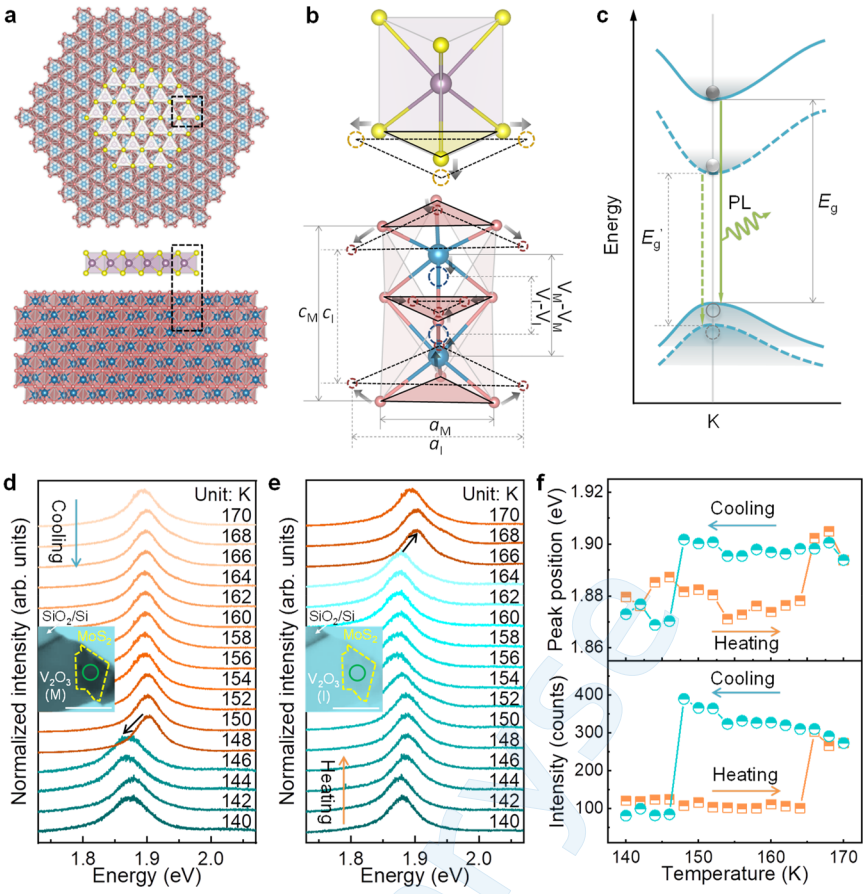


**Figure 6. Strain effect on $MoS_2$monolayer in $MoS_2/V_2O_3$heterostructure. a, Atomic schematic of the $MoS_2/V_2O_3$ heterostructure. Upper panel is a top view, and lower panel is a side view. b, Movements of atoms in the heterostructure (bird's-eye view of black dashed rectangles in a) during the metal−insulator transition of $V_2O_3$. The lattice expansion in the insulating phase of $V_2O_3$ (red and blue dashed circles) induces a tensile biaxial strain in the $MoS_2$ monolayer (yellow dashed circles). c, Redshift of PL/band gap ($E_g$ to $E_g'$) in the $MoS_2$ monolayer induced by the tensile biaxial strain. d,e, PL spectra of the $MoS_2$ monolayer during the metal−insulator transition of the $V_2O_3$ sheet (cooling (d) and heating (e)). The abrupt changes are indicated by black arrows. Insets show optical images of the heterostructure. The color change indicates the metal (dark, M)-insulator (light, I) transition. The $MoS_2$ monolayer is outlined in yellow dashed lines. f, Temperature-dependent PL peak position (upper panel) and intensity (lower panel) extracted from d and e. Scale bars in the insets of d and e: 5 $\mu$m.**

The devices in the bottom-left inset of Figure 5a (device #1) and SI Figure S15a (device #4) have a vertical configuration (sketched in the middle-left inset of Figure 5a, the bottom FLG is between the $V_2O_3$ sheet and substrate). The device in SI Figure S15c (device #5) has a planar configuration with a BN sheet underneath. Due to the van der Waals interaction, these devices may have single-domain behavior during measurements. Indeed, single resistance jumps are observed (Figure 5a and SI Figures S15b,d). The devices in the top-right inset of Figure 5b (device #2) and SI Figures S16a,c (devices #6, #7) have a planar configuration (sketched in the middle-left inset of Figure 5b, both FLGs are on the top of the $V_2O_3$ sheet, and the sheet is directly transferred on the substrate). Thus, the sheet−substrate interactions are relatively stronger than the van der Waals interaction, and these devices may have a multiple-domain behavior during the measurement, as indicated by the multiple resistance jumps in Figure 5b and SI Figures S16b,d (cyan curves). When they are measured for a second cooling−heating cycle, the sheet−substrate interaction may be relieved. As a result, the multiple resistance jumps may disappear, as shown in the orange plots in SI Figures S16b,d. We need to mention that changing both cooling and heating rates from 1 to 20 K/min hardly affects the heterosys behavior, as shown in SI Figures S15d,17 for device #5.

In addition to temperature, the metal−insulator transition in $V_2O_3$ can also be driven by voltage or power.[32] Figures 5c and d show the logarithmic current−voltage and resistance-voltage curves measured at different temperatures, respectively, for device #3 (inset of Figure 5c). The abrupt current/resistance change is observed at 160 K with an applied voltage of ∼2 V. Here, this voltage-induced resistance change is probably triggered by Joule heating.[32]

By taking advantage of the large lattice expansions of 0.74% along ***a*** and 1.22% along ***b*** in the metallic phase of $V_2O_3$ when it changes to the insulating phase, here through the same 2D/3D heterostructure, we demonstrate a strategy to study the effect of strain on the 2D material. We use a $MoS_2$ monolayer as a model 2D material. Figure 6a shows the top view (upper panel) and side view (bottom panel) of an atomic schematic of the $MoS_2/V_2O_3$ heterostructure. Figure 6b (enlarged view of dashed rectangles in Figure 6a) illustrates the movements of atoms in $V_2O_3$ during the metal−insulator transition (dashed circles are for the insulating phase), inducing a biaxial tensile strain in the upper $MoS_2$ monolayer. Since the deformation potential of $MoS_2$ is negative,[66] this biaxial tensile strain can lead to a reduced band gap $E_g$ (redshift of photoluminance (PL)),[67,68] as sketched in Figure 6c.



https://doi.org/10.1021/acsnano.3c02649
ACS Nano 2023, 17, 11783−11793

To fabricate the $MoS_2/V_2O_3$ heterostructure, we exfoliate a $MoS_2$ monolayer from a bulk crystal and then transfer it onto the surface of a $V_2O_3$ sheet using the dry transfer technique. The optical microscopy images of SI Figures S18a,b and insets of Figures 6d,e display the fabricated heterostructure. Figures 6d and e show PL spectra of the $MoS_2$ monolayer at different temperatures during cooling and heating, respectively. When the temperature decreases to 146 K (or increases to 166 K), the $V_2O_3$ sheet undergoes a phase transition (color change in SI Figures S18a,b and insets of Figures 6d,e) accompanied by an abrupt redshift (blueshift) in the PL spectrum. We extract peak positions of all spectra and plot them in the top panel of Figure 6f. The temperature-dependent PL peak position shows a distinct hysteresis. It clearly demonstrates the successful band gap shift of the $MoS_2$ monolayer via the metal−insulator transition of the $V_2O_3$ sheet in the $MoS_2/V_2O_3$ heterostructure. The redshift of the band gap is about 25 meV, corresponding to ∼0.25% biaxial tensile strain in the $MoS_2$ monolayer (a tuning rate of band gap of 99 meV/% is used[67]). Besides, during the phase transition, the PL intensity is greatly reduced/enhanced (about 3−4 times), as shown in the lower panel of Figure 6f. This change is much larger than other experimental values[67,69] and theoretical predictions.[70] The abnormal high PL intensity for the $MoS_2$ monolayer on the metallic phase of $V_2O_3$ sheet may be related to a plasmonic effect[71] but currently remains unclear. A similar band gap shift of the $MoS_2$ monolayer can also be found in another $MoS_2/V_2O_3$ heterostructure, as shown in SI Figures S19a−d.

## CONCLUSIONS

In summary, we unveil the intrinsic domain structure and metal−insulator phase transition kinetics of strongly correlated oxide $V_2O_3$ through interface engineering. We show that with a moderate sheet−substrate coupling strength the insulator/metal domain exhibits stripped trigonal structure intrinsic to the pseudohexagon symmetry of $V_2O_3$. We demonstrate that van der Waals interface engineering could regulate the phase transition kinetics and control the transport characteristics of $V_2O_3$-based metal−insulator switching devices. The van der Waals interface has also been found enabling reciprocal effect on the 2D material−leading to pronounced change on the optical gap of the 2D layer. Our work opens an avenue for engineering the phase transition kinetics of strongly correlated materials allowing effective tuning of operation characteristics of future Mott devices.

## METHODS

**Molecular Dynamics Simulation.** See the details in Supporting Information.

**Synthesis.** We used the flux method to grow single $V_2O_3$ single crystals. First, we filled a 5 mL graphite crucible with 0.2 g of $V_2O_5$ powder (≥99.6%, MilliporeSigma) and 3.28 g of anhydrous KCl (≥99.5%, MilliporeSigma) and then placed it in an alumina tube inside a furnace. Second, we evacuated the tube to 0.1 Torr and then filled it with $H_2$(5%)/Ar gas. We maintained a steady flow of 50 sccm $H_2$(5%)/Ar at one atm throughout the growth. Third, we heated the crucible at 20 °C $min^{-1}$ to 900 °C and kept it for 10 h and then lowered it at 0.5 °C $min^{-1}$ to room temperature. Finally, we washed the contents of the crucible in water (to dissolve the KCl) and obtained a large amount of black shiny crystals with a sheet-like shape.

**Structural Characterizations.** We performed X-ray diffraction with a Panalytical X'Pert PRO MPD system (with a Cu K$\alpha$ source and a PIXcel solid-state line detector). $\omega$-2$\theta$ scans were acquired with a divergent beam Bragg−Brentano geometry over a 2$\theta$ range from 20−80°. We studied vibration modes of $V_2O_3$ sheets by using a WITec Alpha 300 confocal Raman microscope with an excitation source of CW 532 nm.

**Microscopy Characterizations.** We characterized the morphology of $V_2O_3$ sheets by using a Nikon Eclipse Ti−S inverted optical microscope. We used a Multimode TM Atomic Force Microscope to characterize the surface and the thickness of $V_2O_3$ sheets. We collected the high-resolution transmission electron microscopy images and electron diffraction patterns of $V_2O_3$ sheets by using an FEI F20 TEM operated at 200 kV.

**Sheet Transfer.** To select sheets with relatively strong bonding with the substrate, we used a dry transfer technique (all-dry viscoelastic stamping). First, we used a polydimethylsiloxane (PDMS) stamp to pick up sheets from the substrate (press and fast release). Then, we loaded the PDMS stamp with sheets onto a three-axis micro manipulator which was installed on an optical microscope (a home-built 2D material transfer system). Next, we located the sheets having a smooth surface and pressed the stamp on another substrate by using the micromanipulator on an optical microscope. Finally, we gently released the PDMS stamp. The sheets that can be attached on the substrate after releasing the PDMS stamp are expected to have relatively strong bonding with the substrate. We cleaned the surfaces of both substrate and sheet by annealing at 200 °C in vacuum and argon plasma etching. There is no residual PDMS up to the detection limit of XPS,[72] as shown in SI Figure S21.

**Device and Heterostructure Fabrications.** We used the dry transfer technique to fabricate $V_2O_3$ sheet based two-terminal devices with two few-layer graphenes (FLGs) as electrical contacts (FLG/$V_2O_3$/FLG) on metal-patterned substrates. First, we used maskless lithography (Intelligent Micro Patterning model SF-100 Lightning Plus, positive photoresist S1813) to draw a pattern (channel distances of 20 and 30 $\mu$m) on a $SiO_2$ (∼300 nm)/Si(100) substrate. Then, we deposited a Ti (3 nm)/Au (20 nm) layer onto the photoresists-patterned substrate by using the e-beam evaporation. After a lift-off process, we developed the Ti/Au-patterned substrate. Second, we dispersed the as-grown $V_2O_3$ sheets in ethanol and dripped them on a Si(100) substrate. We pressed a PDMS stamp on the substrate and then released. A few sheets were attached on the stamp surface. Third, we exfoliated a graphite crystal into FLGs by using scotch tape and then transferred the FLGs onto a PDMS stamp. Fourthly, we loaded the PDMS stamps with $V_2O_3$ sheets and FLGs onto a three-axis micromanipulator, which is installed on an optical microscope. By using this manipulator, we aligned and attached the $V_2O_3$ sheets and FLGs to the desired positions on the Ti/Au-patterned substrate. After we gently released the PDMS stamps, we finally fabricated FLG/$V_2O_3$/FLG devices. We controlled the device configurations (vertical and lateral) by the transfer sequence and alignment of the $V_2O_3$ sheets and FLGs. Here we need to mention that, because most as-grown sheets are not very thin (from a hundred nanometers to several micrometers), the transfer of a sheet from the PDMS stamp onto a substrate is challenge. In order to increase the success rate of the transfer, thin sheets (below 1 $\mu$m) with a flat, clean surface are favored. In addition, the transfer of the FLG on the top of the sheet (again due to the large thickness of the sheet) is also challenging. The release direction of the PDMS stamp is critical for successful fabrication of the top electrode. To fabricate the $MoS_2/V_2O_3$ heterostructures, first, we exfoliated a bulk $MoS_2$ crystal into monolayers by using scotch tape and then transferred the monolayers onto a PDMS stamp. By using the same 2D transfer system, we transferred a monolayer onto a $V_2O_3$ sheet and finally fabricated a heterostructure.

**Transport and Photoluminance Measurements.** We measured $I$−$V$ and $I$−$t$ curves by using an Autolab PGSTAT302N potentiostat. We measured photoluminance spectra by using a WITec Alpha 300 confocal Raman microscope with an excitation source of CW 532 nm. We used a cryostage (THMS600, Linkam Scientific Instruments Ltd.) to change and maintain the temperature of the devices and heterostructures during the transport and photoluminance measurements. The cooling and heating rate were kept


https://doi.org/10.1021/acsnano.3c02649
ACS Nano 2023, 17, 11783−11793

at 1 K/min for all measurements except for the results in SI Figure S17 (2, 5, and 20 K/min).

## ASSOCIATED CONTENT

### Supporting Information

The Supporting Information is available free of charge at https://pubs.acs.org/doi/10.1021/acsnano.3c02649.

Video S1: domain evolutions of single-crystal $V_2O_3$ sheets (MP4)

Video S2: domain evolutions of single-crystal $V_2O_3$ sheets (MP4)

Video S3: domain evolutions of single-crystal $V_2O_3$ sheets (MP4)

Video S4: simulation results for strong interaction (MP4)

Video S5: simulation results for van der Waals interaction (MP4)

Simulation Method and Simulation Discussion sections for molecular dynamics simulations; Figures S1−S4 for the growth and morphology of single-crystal $V_2O_3$ sheets; Figures S4−S8 for structural characterizations; Figures S9−S12 for domain evolutions; Figures S13, S20 and Table S1 for the results, potential energy, and parameters for molecular dynamics simulations, respectively; Figures S14−S17 for the transport study (metal−insulator transition); Figures S18−S19 for the strain effect of phase transition of $V_2O_3$; Figure S21 for the XPS results (PDF)

## AUTHOR INFORMATION


### Corresponding Authors

**Jie Jiang** − *Department of Materials Science and Engineering, Rensselaer Polytechnic Institute, Troy, New York 12180, United States*; Email: jiangj2@rpi.edu

**Yunfeng Shi** − *Department of Materials Science and Engineering, Rensselaer Polytechnic Institute, Troy, New York 12180, United States*; orcid.org/0000-0003-1700-6049; Email: shiy2@rpi.edu

**Jian Shi** − *Department of Materials Science and Engineering, Rensselaer Polytechnic Institute, Troy, New York 12180, United States*; orcid.org/0000-0003-2115-2225; Email: shij4@rpi.edu

### Authors

**Lifu Zhang** − *Department of Materials Science and Engineering, Rensselaer Polytechnic Institute, Troy, New York 12180, United States*

**Yang Hu** − *Department of Materials Science and Engineering, Rensselaer Polytechnic Institute, Troy, New York 12180, United States*

**Yuwei Guo** − *Department of Materials Science and Engineering, Rensselaer Polytechnic Institute, Troy, New York 12180, United States*

**Zhizhong Chen** − *Department of Materials Science and Engineering, Rensselaer Polytechnic Institute, Troy, New York 12180, United States*

**Ru Jia** − *Department of Materials Science and Engineering, Rensselaer Polytechnic Institute, Troy, New York 12180, United States*

**Saloni Pendse** − *Department of Materials Science and Engineering, Rensselaer Polytechnic Institute, Troy, New York 12180, United States*

**Yu Xiang** − *Department of Physics, Applied Physics and Astronomy, Rensselaer Polytechnic Institute, Troy, New York 12180, United States*

**Gwo-Ching Wang** − *Department of Physics, Applied Physics and Astronomy, Rensselaer Polytechnic Institute, Troy, New York 12180, United States*

Complete contact information is available at: https://pubs.acs.org/10.1021/acsnano.3c02649


### Author Contributions

#J.J. and L.Z. contributed equally to this work. J.J. and J.S. conceived the idea and designed the experiments. Y.S. performed MD simulations. J.J. and L.Z. conducted flux growth, grew samples, and fabricated devices/heterostructures. Z.C. assisted the material growth. J.J., L.Z. and Y.H. performed Raman, optical microscopy, and transport measurements. L.Z. performed XPS measurements. L.Z. and Y.X. performed AFM measurements. Y.G. and J.J. performed TEM characterizations. R.J. performed XRD measurements. S.P. assisted the analysis on domain dynamics. J.J., L.Z. and J.S. analyzed the data and interpreted the results. All the authors were involved in the discussion for data analysis. J.J. and Y.S. prepared the initial draft. J.S. revised the manuscript. J.S. supervised the project.

### Notes

The authors declare no competing financial interest.

## ACKNOWLEDGMENTS

The work is supported by the Air Force Office of Scientific Research under award number FA9550-18-1-0116 and the NYSTAR Focus Center at Rensselaer Polytechnic Institute under award number C180117. This work is also partially supported by the US National Science Foundation under award nos. 1916652, 2031692, and 2024972. This paper is also supported by the U.S. National Science Foundation [Platform for the Accelerated Realization, Analysis, and Discovery of Interface Materials (PARADIM)] under Cooperative Agreement No. DMR-2039380 and made use of the Cornell Center for Materials Research (CCMR) Shared Facilities, which are supported through the NSF MRSEC Program (No. DMR-1719875).

## REFERENCES


(1) Schlom, D. G.; Chen, L.-Q.; Fennie, C. J.; Gopalan, V.; Muller, D. A.; Pan, X.; Ramesh, R.; Uecker, R. Elastic Strain Engineering of Ferroic Oxides. *MRS Bull.* **2014**, *39*, 118−130.

(2) Hyun, S.; Char, K. Effects of Strain on the Dielectric Properties of Tunable Dielectric $SrTiO_3$ Thin Films. *Appl. Phys. Lett.* **2001**, *79*, 254−256.

(3) Wang, Q.-Y.; Li, Z.; Zhang, W.-H.; Zhang, Z.-C.; Zhang, J.-S.; Li, W.; Ding, H.; Ou, Y.-B.; Deng, P.; Chang, K.; Wen, J.; Song, C.-L.; He, K.; Jia, J.-F.; Ji, S.-H.; Wang, Y.-Y.; Wang, L.-L.; Chen, X.; Ma, X.-C.; Xue, Q.-K. Interface-Induced High-Temperature Superconductivity in Single Unit-Cell Fese Films on $SrTiO_3$. *Chin. Phys. Lett.* **2012**, *29*, 037402.

(4) Phillips, J. M. Substrate Selection for High-Temperature Superconducting Thin Films. *J. Appl. Phys.* **1996**, *79*, 1829−1848.

(5) Choi, K. J.; Biegalski, M.; Li, Y. L.; Sharan, A.; Schubert, J.; Uecker, R.; Reiche, P.; Chen, Y. B.; Pan, X. Q.; Gopalan, V.; Chen, L.-Q.; Schlom, D. G.; Eom, C. B. Enhancement of Ferroelectricity in Strained $BaTiO_3$ Thin Films. *Science* **2004**, *306*, 1005−1009.

(6) Haeni, J. H.; Irvin, P.; Chang, W.; Uecker, R.; Reiche, P.; Li, Y. L.; Choudhury, S.; Tian, W.; Hawley, M. E.; Craigo, B.; Tagantsev, A. K.; Pan, X. Q.; Streiffer, S. K.; Chen, L. Q.; Kirchoefer, S. W.; Levy, J.;

Schlom, D. G. Room-Temperature Ferroelectricity in Strained $SrTiO_3$. *Nature* **2004**, *430*, 758−761.
(7) Harrington, S. A.; Zhai, J.; Denev, S.; Gopalan, V.; Wang, H.; Bi, Z.; Redfern, S. A. T.; Baek, S.-H.; Bark, C. W.; Eom, C.-B.; Jia, Q.; Vickers, M. E.; MacManus-Driscoll, J. L. Thick Lead-Free Ferroelectric Films with High Curie Temperatures through Nanocomposite-Induced Strain. *Nat. Nanotechnol.* **2011**, *6*, 491−495.
(8) Wang, J.; Neaton, J. B.; Zheng, H.; Nagarajan, V.; Ogale, S. B.; Liu, B.; Viehland, D.; Vaithyanathan, V.; Schlom, D. G.; Waghmare, U. V.; Spaldin, N. A.; Rabe, K. M.; Wuttig, M.; Ramesh, R. Epitaxial $BiFeO_3$ Multiferroic Thin Film Heterostructures. *Science* **2003**, *299*, 1719−1722.
(9) Lee, J. H.; Fang, L.; Vlahos, E.; Ke, X. L.; Jung, Y. W.; Kourkoutis, L. F.; Kim, J. W.; Ryan, P. J.; Heeg, T.; Roeckerath, M.; Goian, V.; Bernhagen, M.; Uecker, R.; Hammel, P. C.; Rabe, K. M.; Kamba, S.; Schubert, J.; Freeland, J. W.; Muller, D. A.; Fennie, C. J.; et al. A Strong Ferroelectric Ferromagnet Created by Means of Spin-Lattice Coupling. *Nature* **2010**, *466*, 954−958.
(10) Locquet, J. P.; Perret, J.; Fompeyrine, J.; Machler, E.; Seo, J. W.; Van Tendeloo, G. Doubling the Critical Temperature of $La_{1.9}Sr_{0.1}CuO_4$ Using Epitaxial Strain. *Nature* **1998**, *394*, 453−456.
(11) Ahadi, K.; Galletti, L.; Li, Y.; Salmani-Rezaie, S.; Wu, W.; Stemmer, S. Enhancing Superconductivity in $SrTiO_3$ Films with Strain. *Sci. Adv.* **2019**, *5*, No. eaaw0120.
(12) Hicks, C. W.; Brodsky, D. O.; Yelland, E. A.; Gibbs, A. S.; Bruin, J. A. N.; Barber, M. E.; Edkins, S. D.; Nishimura, K.; Yonezawa, S.; Maeno, Y.; Mackenzie, A. P. Strong Increase of $T_c$ of $Sr_2RuO_4$ under Both Tensile and Compressive Strain. *Science* **2014**, *344*, 283−285.
(13) Lee, D.; Chung, B.; Shi, Y.; Kim, G.-Y.; Campbell, N.; Xue, F.; Song, K.; Choi, S.-Y.; Podkaminer, J. P.; Kim, T. H.; Ryan, P. J.; Kim, J.-W.; Paudel, T. R.; Kang, J.-H.; Spinuzzi, J. W.; Tenne, D. A.; Tsymbal, E. Y.; Rzchowski, M. S.; Chen, L. Q.; Lee, J.; et al. Isostructural Metal-Insulator Transition in $VO_2$. *Science* **2018**, *362*, 1037−1040.
(14) Jeong, J.; Aetukuri, N.; Graf, T.; Schladt, T. D.; Samant, M. G.; Parkin, S. S. P. Suppression of Metal-Insulator Transition in $VO_2$ by Electric Field-Induced Oxygen Vacancy Formation. *Science* **2013**, *339*, 1402−1405.
(15) Aetukuri, N. B.; Gray, A. X.; Drouard, M.; Cossale, M.; Gao, L.; Reid, A. H.; Kukreja, R.; Ohldag, H.; Jenkins, C. A.; Arenholz, E.; Roche, K. P.; Duerr, H. A.; Samant, M. G.; Parkin, S. S. P. Control of the Metal-Insulator Transition in Vanadium Dioxide by Modifying Orbital Occupancy. *Nat. Phys.* **2013**, *9*, 661−666.
(16) Cao, J.; Ertekin, E.; Srinivasan, V.; Fan, W.; Huang, S.; Zheng, H.; Yim, J. W. L.; Khanal, D. R.; Ogletree, D. F.; Grossman, J. C.; Wu, J. Strain Engineering and One-Dimensional Organization of Metal-Insulator Domains in Single-Crystal Vanadium Dioxide Beams. *Nat. Nanotechnol.* **2009**, *4*, 732−737.
(17) Wei, J.; Wang, Z.; Chen, W.; Cobden, D. H. New Aspects of the Metal-Insulator Transition in Single-Domain Vanadium Dioxide Nanobeams. *Nat. Nanotechnol.* **2009**, *4*, 420−424.
(18) Cao, J.; Gu, Y.; Fan, W.; Chen, L. Q.; Ogletree, D. F.; Chen, K.; Tamura, N.; Kunz, M.; Barrett, C.; Seidel, J.; Wu, J. Extended Mapping and Exploration of the Vanadium Dioxide Stress-Temperature Phase Diagram. *Nano Lett.* **2010**, *10*, 2667−2673.
(19) Park, J. H.; Coy, J. M.; Kasirga, T. S.; Huang, C.; Fei, Z.; Hunter, S.; Cobden, D. H. Measurement of a Solid-State Triple Point at the Metal-Insulator Transition in $VO_2$. *Nature* **2013**, *500*, 431−434.
(20) Kasırga, T. S.; Sun, D.; Park, J. H.; Coy, J. M.; Fei, Z.; Xu, X.; Cobden, D. H. Photoresponse of a Strongly Correlated Material Determined by Scanning Photocurrent Microscopy. *Nat. Nanotechnol.* **2012**, *7*, 723−727.
(21) Lee, S.; Hippalgaonkar, K.; Yang, F.; Hong, J.; Ko, C.; Suh, J.; Liu, K.; Wang, K.; Urban, J. J.; Zhang, X.; Dames, C.; Hartnoll, S. A.; Delaire, O.; Wu, J. Anomalously Low Electronic Thermal Conductivity in Metallic Vanadium Dioxide. *Science* **2017**, *355*, 371−374.
(22) Ji, D.; Cai, S.; Paudel, T. R.; Sun, H.; Zhang, C.; Han, L.; Wei, Y.; Zang, Y.; Gu, M.; Zhang, Y.; Gao, W.; Huyan, H.; Guo, W.; Wu, D.; Gu, Z.; Tsymbal, E. Y.; Wang, P.; Nie, Y.; Pan, X. Freestanding Crystalline Oxide Perovskites Down to the Monolayer Limit. *Nature* **2019**, *570*, 87−90.
(23) Dong, G.; Li, S.; Yao, M.; Zhou, Z.; Zhang, Y.-Q.; Han, X.; Luo, Z.; Yao, J.; Peng, B.; Hu, Z.; Huang, H.; Jia, T.; Li, J.; Ren, W.; Ye, Z.-G.; Ding, X.; Sun, J.; Nan, C.-W.; Chen, L.-Q.; Li, J.; et al. Super-Elastic Ferroelectric Single-Crystal Membrane with Continuous Electric Dipole Rotation. *Science* **2019**, *366*, 475−479.
(24) McWhan, D. B.; Remeika, J. P. Metal-Insulator Transition in $(V_{1-x}Cr_x)_2O_3$. *Phys. Rev. B* **1970**, *2*, 3734−3750.
(25) Dernier, P. D. The Crystal Structure of $V_2O_3$ and $(V_{0.962}Cr_{0.038})_2O_3$ near the Metal-Insulator Transition. *J. Phys. Chem. Solids* **1970**, *31*, 2569−2575.
(26) Feinleib, J.; Paul, W. Semiconductor-to-Metal Transition in $V_2O_3$. *Phys. Rev.* **1967**, *155*, 841−850.
(27) Morin, F. J. Oxides Which Show a Metal-to-Insulator Transition at the Neel Temperature. *Phys. Rev. Lett.* **1959**, *3*, 34−36.
(28) Imada, M.; Fujimori, A.; Tokura, Y. Metal-Insulator Transitions. *Rev. Mod. Phys.* **1998**, *70*, 1039−1263.
(29) Mott, N. F. Metal-Insulator Transition. *Rev. Mod. Phys.* **1968**, *40*, 677−683.
(30) Hansmann, P.; Toschi, A.; Sangiovanni, G.; Saha-Dasgupta, T.; Lupi, S.; Marsi, M.; Held, K. Mott-Hubbard Transition in $V_2O_3$ Revisited. *Phys. Status Solidi B* **2013**, *250*, 1251−1264.
(31) McLeod, A. S.; van Heumen, E.; Ramirez, J. G.; Wang, S.; Saerbeck, T.; Guenon, S.; Goldflam, M.; Anderegg, L.; Kelly, P.; Mueller, A.; Liu, M. K.; Schuller, I. K.; Basov, D. N. Nanotextured Phase Coexistence in the Correlated Insulator $V_2O_3$. *Nat. Phys.* **2017**, *13*, 80−86.
(32) Brockman, J. S.; Gao, L.; Hughes, B.; Rettner, C. T.; Samant, M. G.; Roche, K. P.; Parkin, S. S. P. Subnanosecond Incubation Times for Electric-Field-Induced Metallization of a Correlated Electron Oxide. *Nat. Nanotechnol.* **2014**, *9*, 453−458.
(33) Lupi, S.; Baldassarre, L.; Mansart, B.; Perucchi, A.; Barinov, A.; Dudin, P.; Papalazarou, E.; Rodolakis, F.; Rueff, J. -P.; Itie, J. -P.; Ravy, S.; Nicoletti, D.; Postorino, P.; Hansmann, P.; Parragh, N.; Toschi, A.; Saha-Dasgupta, T.; Andersen, O. K.; Sangiovanni, G.; Held, K.; Marsi, M. A Microscopic View on the Mott Transition in Chromium-Doped $V_2O_3$. *Nat. Commun.* **2010**, *1*, 105.
(34) Rodolakis, F.; Hansmann, P.; Rueff, J. P.; Toschi, A.; Haverkort, M. W.; Sangiovanni, G.; Tanaka, A.; Saha-Dasgupta, T.; Andersen, O. K.; Held, K.; Sikora, M.; Alliot, I.; Itié, J. P.; Baudelet, F.; Wzietek, P.; Metcalf, P.; Marsi, M. Inequivalent Routes across the Mott Transition in $V_2O_3$ Explored by X-Ray Absorption. *Phys. Rev. Lett.* **2010**, *104*, 047401.
(35) Liu, M. K.; Pardo, B.; Zhang, J.; Qazilbash, M. M.; Yun, S. J.; Fei, Z.; Shin, J.-H.; Kim, H.-T.; Basov, D. N.; Averitt, R. D. Photoinduced Phase Transitions by Time-Resolved Far-Infrared Spectroscopy in $V_2O_3$. *Phys. Rev. Lett.* **2011**, *107*, 066403.
(36) Frandsen, B. A.; Liu, L.; Cheung, S. C.; Guguchia, Z.; Khasanov, R.; Morenzoni, E.; Munsie, T. J. S.; Hallas, A. M.; Wilson, M. N.; Cai, Y.; Luke, G. M.; Chen, B.; Li, W.; Jin, C.; Ding, C.; Guo, S.; Ning, F.; Ito, T. U.; Higemoto, W.; Billinge, S. J. L.; et al. Volume-Wise Destruction of the Antiferromagnetic Mott Insulating State through Quantum Tuning. *Nat. Commun.* **2016**, *7*, 12519.
(37) Lantz, G.; Mansart, B.; Grieger, D.; Boschetto, D.; Nilforoushan, N.; Papalazarou, E.; Moisan, N.; Perfetti, L.; Jacques, V. L. R.; Le Bolloc'h, D.; Laulhé, C.; Ravy, S.; Rueff, J. P.; Glover, T. E.; Hertlein, M. P.; Hussain, Z.; Song, S.; Chollet, M.; Fabrizio, M.; Marsi, M. Ultrafast Evolution and Transient Phases of a Prototype out-of-Equilibrium Mott-Hubbard Material. *Nat. Commun.* **2017**, *8*, 13917.
(38) Qazilbash, M. M.; Schafgans, A. A.; Burch, K. S.; Yun, S. J.; Chae, B. G.; Kim, B. J.; Kim, H. T.; Basov, D. N. Electrodynamics of the Vanadium Oxides $VO_2$ and $V_2O_3$. *Phys. Rev. B* **2008**, *77*, 115121.
(39) Stewart, M. K.; Brownstead, D.; Wang, S.; West, K. G.; Ramirez, J. G.; Qazilbash, M. M.; Perkins, N. B.; Schuller, I. K.; Basov,


https://doi.org/10.1021/acsnano.3c02649
*ACS Nano* 2023, 17, 11783−11793

D. N. Insulator-to-Metal Transition and Correlated Metallic State of $V_2O_3$ Investigated by Optical Spectroscopy. *Phys. Rev. B* **2012**, *85*, 205113.
(40) Lo Vecchio, I.; Baldassarre, L.; D'Apuzzo, F.; Limaj, O.; Nicoletti, D.; Perucchi, A.; Fan, L.; Metcalf, P.; Marsi, M.; Lupi, S. Optical Properties of $V_2O_3$ in Its Whole Phase Diagram. *Phys. Rev. B* **2015**, *91*, 155133.
(41) Laad, M. S.; Craco, L.; Müller-Hartmann, E. Orbital-Selective Insulator-Metal Transition in $V_2O_3$ under External Pressure. *Phys. Rev. B* **2006**, *73*, 045109.
(42) Ezhov, S. Y.; Anisimov, V. I.; Khomskii, D. I.; Sawatzky, G. A. Orbital Occupation, Local Spin, and Exchange Interactions in $V_2O_3$. *Phys. Rev. Lett.* **1999**, *83*, 4136−4139.
(43) Poteryaev, A. I.; Tomczak, J. M.; Biermann, S.; Georges, A.; Lichtenstein, A. I.; Rubtsov, A. N.; Saha-Dasgupta, T.; Andersen, O. K. Enhanced Crystal-Field Splitting and Orbital-Selective Coherence Induced by Strong Correlations in $V_2O_3$. *Phys. Rev. B* **2007**, *76*, 085127.
(44) Ronchi, A.; Homm, P.; Menghini, M.; Franceschini, P.; Maccherozzi, F.; Banfi, F.; Ferrini, G.; Cilento, F.; Parmigiani, F.; Dhesi, S. S.; Fabrizio, M.; Locquet, J. P.; Giannetti, C. Early-Stage Dynamics of Metallic Droplets Embedded in the Nanotextured Mott Insulating Phase of $V_2O_3$. *Phys. Rev. B* **2019**, *100*, 075111.
(45) Ronchi, A.; Franceschini, P.; De Poli, A.; Homm, P.; Fitzpatrick, A.; Maccherozzi, F.; Ferrini, G.; Banfi, F.; Dhesi, S. S.; Menghini, M.; Fabrizio, M.; Locquet, J.-P.; Giannetti, C. Nanoscale Self-Organization and Metastable Non-Thermal Metallicity in Mott Insulators. *Nat. Commun.* **2022**, *13*, 3730.
(46) Tran, R.; Li, X.-G.; Ong, S. P.; Kalcheim, Y.; Schuller, I. K. Metal-Insulator Transition in $V_2O_3$ with Intrinsic Defects. *Phys. Rev. B* **2021**, *103*, 075134.
(47) del Valle, J.; Ghazikhanian, N.; Kalcheim, Y.; Trastoy, J.; Lee, M.-H.; Rozenberg, M. J.; Schuller, I. K. Resistive Asymmetry Due to Spatial Confinement in First-Order Phase Transitions. *Phys. Rev. B* **2018**, *98*, 045123.
(48) Kalcheim, Y.; Camjayi, A.; del Valle, J.; Salev, P.; Rozenberg, M.; Schuller, I. K. Non-Thermal Resistive Switching in Mott Insulator Nanowires. *Nat. Commun.* **2020**, *11*, 2985.
(49) Lantz, G.; Hajlaoui, M.; Papalazarou, E.; Jacques, V. L. R.; Mazzotti, A.; Marsi, M.; Lupi, S.; Amati, M.; Gregoratti, L.; Si, L.; Zhong, Z.; Held, K. Surface Effects on the Mott-Hubbard Transition in Archetypal $V_2O_3$. *Phys. Rev. Lett.* **2015**, *115*, 236802.
(50) del Valle, J.; Vargas, N. M.; Rocco, R.; Salev, P.; Kalcheim, Y.; Lapa, P. N.; Adda, C.; Lee, M.-H.; Wang, P. Y.; Fratino, L.; Rozenberg, M. J.; Schuller, I. K. Spatiotemporal Characterization of the Field-Induced Insulator-to-Metal Transition. *Science* **2021**, *373*, 907−911.
(51) Charlier, J. C.; Gonze, X.; Michenaud, J. P. Graphite Interplanar Bonding: Electronic Eelocalization and Van Der Waals Interaction. *Europhysics Letters (EPL)* **1994**, *28*, 403−408.
(52) Kong, W.; Li, H.; Qiao, K.; Kim, Y.; Lee, K.; Nie, Y.; Lee, D.; Osadchy, T.; Molnar, R. J.; Gaskill, D. K.; Myers-Ward, R. L.; Daniels, K. M.; Zhang, Y.; Sundram, S.; Yu, Y.; Bae, S.-h.; Rajan, S.; Shao-Horn, Y.; Cho, K.; Ougazzaden, A.; et al. Polarity Governs Atomic Interaction through Two-Dimensional Materials. *Nat. Mater.* **2018**, *17*, 999−1004.
(53) Chae, S.; Jang, S.; Choi, W. J.; Kim, Y. S.; Chang, H.; Lee, T. I.; Lee, J.-O. Lattice Transparency of Graphene. *Nano Lett.* **2017**, *17*, 1711−1718.
(54) Kuroda, N.; Fan, H. Y. Raman Scattering and Phase Transitions of $V_2O_3$. *Phys. Rev. B* **1977**, *16*, 5003−5008.
(55) Wu, J.; Gu, Q.; Guiton, B. S.; de Leon, N. P.; Ouyang, L.; Park, H. Strain-Induced Self Organization of Metal-Insulator Domains in Single-Crystalline $VO_2$ Nanobeams. *Nano Lett.* **2006**, *6*, 2313−2317.
(56) Hadjimichael, M.; Li, Y.; Zatterin, E.; Chahine, G. A.; Conroy, M.; Moore, K.; Connell, E. N. O.; Ondrejkovic, P.; Marton, P.; Hlinka, J.; Bangert, U.; Leake, S.; Zubko, P. Metal-Ferroelectric Supercrystals with Periodically Curved Metallic Layers. *Nat. Mater.* **2021**, *20*, 495−502.
(57) Nahas, Y.; Prokhorenko, S.; Fischer, J.; Xu, B.; Carrétéro, C.; Prosandeev, S.; Bibes, M.; Fusil, S.; Dkhil, B.; Garcia, V.; Bellaiche, L. Inverse Transition of Labyrinthine Domain Patterns in Ferroelectric Thin Films. *Nature* **2020**, *577*, 47−51.
(58) Feigl, L.; Yudin, P.; Stolichnov, I.; Sluka, T.; Shapovalov, K.; Mtebwa, M.; Sandu, C. S.; Wei, X.-K.; Tagantsev, A. K.; Setter, N. Controlled Stripes of Ultrafine Ferroelectric Domains. *Nat. Commun.* **2014**, *5*, 4677.
(59) Kwak, B. S.; Erbil, A.; Wilkens, B. J.; Budai, J. D.; Chisholm, M. F.; Boatner, L. A. Strain Relaxation by Domain Formation in Epitaxial Ferroelectric Thin Films. *Phys. Rev. Lett.* **1992**, *68*, 3733−3736.
(60) Kaganer, V. M.; Jenichen, B.; Schippan, F.; Braun, W.; Däweritz, L.; Ploog, K. H. Strain-Mediated Phase Coexistence in Heteroepitaxial Films. *Phys. Rev. Lett.* **2000**, *85*, 341−344.
(61) Gatel, C.; Warot-Fonrose, B.; Biziere, N.; Rodríguez, L. A.; Reyes, D.; Cours, R.; Castiella, M.; Casanove, M. J. Inhomogeneous Spatial Distribution of the Magnetic Transition in an Iron-Rhodium Thin Film. *Nat. Commun.* **2017**, *8*, 15703.
(62) Parkin, S. S. P.; Hayashi, M.; Thomas, L. Magnetic Domain-Wall Racetrack Memory. *Science* **2008**, *320*, 190−194.
(63) Dho, J.; Kim, Y. N.; Hwang, Y. S.; Kim, J. C.; Hur, N. H. Strain-Induced Magnetic Stripe Domains in $La_{0.7}Sr_{0.3}MnO_3$ Thin Films. *Appl. Phys. Lett.* **2003**, *82*, 1434−1436.
(64) Pendse, S.; Jiang, J.; Zhang, L.; Guo, Y.; Chen, Z.; Hu, Y.; Lu, Z.; Li, S.; Feng, J.; Lu, T.-M.; Shi, J. Tuning Phase Transition Kinetics Via Van Der Waals Epitaxy of Single Crystalline $VO_2$ on Hexagonal-Bn. *J. Cryst. Growth* **2020**, *543*, 125699.
(65) Ding, Y.; Chen, C.-C.; Zeng, Q.; Kim, H.-S.; Han, M. J.; Balasubramanian, M.; Gordon, R.; Li, F.; Bai, L.; Popov, D.; Heald, S. M.; Gog, T.; Mao, H.-k.; van Veenendaal, M. Novel High-Pressure Monoclinic Metallic Phase of $V_2O_3$. *Phys. Rev. Lett.* **2014**, *112*, 056401.
(66) Peelaers, H.; Van de Walle, C. G. Effects of Strain on Band Structure and Effective Masses in $MoS_2$. *Phys. Rev. B* **2012**, *86*, 241401.
(67) Lloyd, D.; Liu, X.; Christopher, J. W.; Cantley, L.; Wadehra, A.; Kim, B. L.; Goldberg, B. B.; Swan, A. K.; Bunch, J. S. Band Gap Engineering with Ultralarge Biaxial Strains in Suspended Monolayer $MoS_2$. *Nano Lett.* **2016**, *16*, 5836−5841.
(68) Feng, J.; Qian, X.; Huang, C.-W.; Li, J. Strain-Engineered Artificial Atom as a Broad-Spectrum Solar Energy Funnel. *Nat. Photonics* **2012**, *6*, 866−871.
(69) Conley, H. J.; Wang, B.; Ziegler, J. I.; Haglund, R. F.; Pantelides, S. T.; Bolotin, K. I. Bandgap Engineering of Strained Monolayer and Bilayer $MoS_2$. *Nano Lett.* **2013**, *13*, 3626−3630.
(70) Steinhoff, A.; Kim, J. H.; Jahnke, F.; Rösner, M.; Kim, D. S.; Lee, C.; Han, G. H.; Jeong, M. S.; Wehling, T. O.; Gies, C. Efficient Excitonic Photoluminescence in Direct and Indirect Band Gap Monolayer $MoS_2$. *Nano Lett.* **2015**, *15*, 6841−6847.
(71) Lee, H. S.; Kim, M. S.; Jin, Y.; Han, G. H.; Lee, Y. H.; Kim, J. Selective Amplification of the Primary Exciton in a $MoS_2$ Monolayer. *Phys. Rev. Lett.* **2015**, *115*, 226801.
(72) Dahiya, R.; Gottardi, G.; Laidani, N. Pdms Residues-Free Micro/Macrostructures on Flexible Substrates. *Microelectron. Eng.* **2015**, *136*, 57−62.


https://doi.org/10.1021/acsnano.3c02649
*ACS Nano* 2023, 17, 11783−11793